

# Model Reduction via Dynamic Mode Decomposition

Hannah Lu<sup>a,1</sup>, Daniel M. Tartakovsky<sup>a,\*</sup>

<sup>a</sup>*Department of Energy Resources Engineering, Stanford University, Stanford, CA 94305, USA*

---

## Abstract

This work proposes a new framework of model reduction for parametric complex systems. The framework employs a popular model reduction technique dynamic mode decomposition (DMD), which is capable of combining data-driven learning and physics ingredients based on the Koopman operator theory. In the offline step of the proposed framework, DMD constructs a low-rank linear surrogate model for the high dimensional quantities of interest (QoIs) derived from the (nonlinear) complex high fidelity models (HFMs) of unknown forms. Then in the online step, the resulting local reduced order bases (ROBs) and parametric reduced order models (PROMs) at the training parameter sample points are interpolated to construct a new PROM with the corresponding ROB for a new set of target/test parameter values. The interpolations need to be done on the appropriate manifolds within consistent sets of generalized coordinates. The proposed framework is illustrated by numerical examples for both linear and nonlinear problems. In particular, its advantages in computational costs and accuracy are demonstrated by the comparisons with projection-based proper orthogonal decomposition (POD)-PROM and Kriging.

*Keywords:* reduced-order modeling; data-driven learning; parametric systems; manifold interpolations

---

## 1. Introduction

Physics-based modeling and simulation is playing a significant role across many applications in engineering and science. Despite continuing advances in software and hardware development, including high-performance computing, high fidelity simulations for complex systems remain a demanding and elusive task. That is especially so in sensitivity analysis, uncertainty quantification, inverse modeling, where many simulation runs are required. Real-time applications (e.g., decision making and optimization) also require the parametric computational models, which represent the underlying dynamics in various scenarios, to be simulated accurately within the limited computational time or capacities.

Model reduction techniques can significantly reduce the (prohibitively) high computational costs of physics-based high fidelity simulations, while capturing the essential features of the underlying dynamics.

---

\*Corresponding author

*Email address:* [tartakovsky@stanford.edu](mailto:tartakovsky@stanford.edu) (Daniel M. Tartakovsky)

<sup>1</sup>email: [hannahlu@stanford.edu](mailto:hannahlu@stanford.edu)

Such techniques have been used extensively in computational engineering and can be grouped in two general classes. The first are physics-based/projection-based approaches (see [1] for a comprehensive review), which seek for a Galerkin projection from a HFM to a representative surrogate model on a low-dimensional “trial” subspace for the system states. A prime example of this class is POD [2, 3] and discrete empirical interpolation (DEIM) [4] for linear and nonlinear systems respectively, both of which are grounded in singular value decomposition (SVD). They obtain the linear trial subspaces determined by the SVD analysis in the time domain. Related approaches in the frequency domain include balanced truncation [5, 6] and rational interpolation [7, 8]. Alternatively, nonlinear trial manifolds can be obtained using deep convolutional autoencoders in a recent work [9]. The computational saving stems from replacing the high-dimensional full system with its lower-dimensional counterpart for future prediction. Such reduced order models (ROMs) are physics-based in the sense that they inherit the (presumably known) dynamic operator from the projection.

As HFMs become increasingly complex and data becomes more available, there is a growing need for data-driven ROMs, which belong to the second class. Instead of making a direct dimension-reduction of the underlying high-fidelity code that produces the data, data-driven ROMs aim to reduce its complexity by learning the dynamics of the state variables or QoIs directly from the full model’s output and/or observational data. Machine learning techniques, such as Gaussian process regression (also known as Kriging or response surface estimation) [10, 11], random forest (RF) [12, 13], dynamic mode decomposition (DMD) [14, 15], operator inference [16, 17] and neural networks (NN) [18, 19], are widely used in the constructions of these data-driven ROMs. Physics ingredients can be embedded in the data-driven learning so that both flexibility and robustness can be enhanced even with limited data accessibility [20, 21, 22, 23, 24, 25, 26, 27, 28].

Many complex systems are designed and analyzed by their dependency on the parameters, which account for variations in shape, material, loading, and boundary and initial conditions. Consequently, the ROMs for these parametric complex systems (known as PROMs) are required to be robust with respect to the variations in parameters. For the first class of physics-based/projection-based PROMs, this issue was discussed in [29, 30, 31, 32] and later resolved in [33, 34] using appropriate interpolations of the ROBs and PROMs on suitable manifolds respectively. Later improvements in interpolation include [35, 36, 37]. The major challenge of the first class PROMs for complex systems is that they are “physics hungry” – the projections can only be designed for the full state variables with full knowledge of the dynamic operators. It is inefficient and sometimes unfeasible to deal with a large number of state variables with their extremely high dimension after spatial discretization and huge systems of (nonlinear) dynamic operators. On the other hand, the second class data-driven PROMs can be “data hungry”. The time evolution of the QoIs, expressed as a function of the parameters and simulated predictors, can present high nonlinearity or/and bifurcations. It becomes challenging for conventional approximators like Gaussian

Regression Process to capture the dynamics precisely as discussed in [34] and verified in our numerical example section 4.3. Modern nonlinear machine learning methods like RF and NN show advantageous performances in this case but only when enough amount of high-fidelity data are available for training [38, 39, 40]. Alternative strategies include operator inference [17], which needs assumptions of polynomial structures on the underlying dynamics.

Given the aforementioned challenges, adapting the data-driven model reduction strategies to the parametric setting is an active area of research. In this work, we propose a physics-aware data-driven DMD-PROM framework, which combines the advantages from both classes of PROMs. The proposed framework consists of two steps: 1). The offline step constructs a low-rank DMD-based (linear) ROM for the observables of the QoIs at each training sample parameter point. The physics-guided selection of observables, which is based on the Koopman operator theory, provides not only better accuracy in the local ROMs, but also a bridge between the understanding of data and physics. 2). The online step constructs a new PROM with corresponding ROB for each target/test parameter point by interpolating the training PROMs and ROBs. The interpolations are done on suitable manifolds in the same fashion as in the projection-based PROMs. Our framework alleviates the constraints on the access to the HFMs in projection-based PROMs and the need for large amount of data in pure data-driven PROMs.

The remainder of the paper is organized as follows. The problem of interest is formulated in section 2. Then we establish the general methodology and summarize the practical algorithms in section 3. In section 4, several numerical examples are presented to demonstrate the accuracy and robustness of the proposed framework, with comparison with other methods. Key results, their implication for applications, and challenges and future work are summarized in section 5.

## 2. Problem Formulation

We consider a complex system that is described by  $N'_{sv}$  state variables  $\mathbf{s}(\mathbf{x}, t; \mathbf{p}) = \{s_1, \dots, s_{N'_{sv}}\}$ , varying in space  $\mathbf{x} \in \mathcal{D}$ , time  $t \in [0, T]$  and parameter  $\mathbf{p} \in \Omega$  throughout the simulation domain  $\mathcal{D}$  during the simulation time interval  $[0, T]$  within the parameter range  $\Omega$ . The spatiotemporal evolution of these state variables is described by a system of coupled partial-differential equations (PDEs)

$$\frac{\partial s_i}{\partial t} = \phi_i(\mathbf{s}; \mathbf{p}), \quad (\mathbf{x}, t) \in \mathcal{D} \times (0, T); \quad i = 1, \dots, N'_{sv}, \quad (2.1)$$

where  $\phi_i$  are (linear/nonlinear) differential operators that contain spatial derivatives, and  $\mathbf{p} = \{p_1, \dots, p_{N_{\text{par}}}\}$  is a set of  $N_{\text{par}}$  parameters. Problems of this kind have to be solved numerically, which requires a discretization of the spatial domain  $\mathcal{D}$  into  $N_{\text{el}}$  elements/nodes, leading to a discretized state variable  $\mathbf{S}(t; \mathbf{p})$  of very high dimension  $N_{sv} = N'_{sv} \times N_{\text{el}}$ , satisfying

$$\frac{d\mathbf{S}}{dt}(t; \mathbf{p}) = \mathbf{\Phi}(\mathbf{S}(t; \mathbf{p}); \mathbf{p}), \quad (2.2)$$

where  $\Phi$  are linear/nonlinear functions.

More often than not, this model output has to be post-processed to compute  $N_Q$  QoIs  $\mathbf{Q}(t; \mathbf{p}) = [Q_1(t; \mathbf{p}), \dots, Q_{N_Q}(t; \mathbf{p})]^\top$ , such that

$$Q_i(t; \mathbf{p}) = \mathcal{M}_i(\mathbf{S}(t; \mathbf{p})), \quad \text{for } i = 1, \dots, N_Q. \quad (2.3)$$

The maps  $\mathcal{M}_i$  can represent, e.g., numerical approximations of the integrals over  $\mathcal{D}$  or a streamline. The QoIs are usually much easier to visualize and comprehend than the raw output  $\mathbf{S}(t; \mathbf{p})$ . We are interested in the HFM for the QoIs

$$\frac{d\mathbf{Q}}{dt}(t; \mathbf{p}) = \mathbf{F}(\mathbf{Q}(t; \mathbf{p}); \mathbf{p}) \quad (2.4)$$

instead of the complex system (2.2) for  $\mathbf{S}(t; \mathbf{p})$ . Notice that the function  $\mathbf{F}$  has a complicated form which depends on the knowledge of the original system (2.2). The corresponding discrete-time dynamical system is described by

$$\mathbf{Q}(t_{k+1}; \mathbf{p}) = \mathbf{F}_{\Delta t}(\mathbf{Q}(t_k; \mathbf{p}); \mathbf{p}) := \mathbf{Q}(t_k; \mathbf{p}) + \int_{t_k}^{t_k + \Delta t} \mathbf{F}(\mathbf{Q}(\tau; \mathbf{p})) d\tau \quad (2.5)$$

for the uniform time discretization  $t_k = k\Delta t \in [0, T], k = 0, \dots, N_T$ .

Given  $N_{\text{snap}}$  snapshots of the trajectories of the QoIs computed from (2.2) and (2.3) at sampled parameter points  $\{\mathbf{p}^{(1)}, \dots, \mathbf{p}^{(N_{\text{MC}})}\}$ ,

$$\{\mathbf{Q}(t_0; \mathbf{p}^{(1)}), \dots, \mathbf{Q}(t_{N_{\text{snap}}}; \mathbf{p}^{(1)}), \dots, \mathbf{Q}(t_0; \mathbf{p}^{(N_{\text{MC}})}), \dots, \mathbf{Q}(t_{N_{\text{snap}}}; \mathbf{p}^{(N_{\text{MC}})})\}, \quad N_{\text{snap}} \leq N_T, \quad (2.6)$$

we aim to construct a surrogate model of reduced dimension for the discretized HFM (2.5). This will allow us to predict the trajectory of the QoIs at an unsampled parameter point  $\mathbf{p}^* \notin \{\mathbf{p}^{(1)}, \dots, \mathbf{p}^{(N_{\text{MC}})}\}$ , i.e.,  $\{\mathbf{Q}(t_0; \mathbf{p}^*), \dots, \mathbf{Q}(t_{N_T}; \mathbf{p}^*)\}$ , directly at a low cost without computing the complex high dimensional system (2.2) and (2.3).

### 3. Methodology

We propose a DMD-PROM framework consisting of the following offline step and online step in section 3.1 and section 3.2 respectively.

#### 3.1. Offline Step: DMD-based Surrogate Models

Without the accessibility to the original system (2.2) and (2.3), one can regard the dynamic function  $\mathbf{F}$  as unknown in (2.4) (and  $\mathbf{F}_{\Delta t}$  unknown in (2.5) correspondingly). The goal of this step is to construct a surrogate linear model of reduced dimension for the unknown discrete HFM (2.5) from the dataset (2.6).

We first review the Koopman operator theory, which allows one to handle the potential nonlinearity in the unknown dynamic  $\mathbf{F}$  and  $\mathbf{F}_{\Delta t}$ :

**Definition 3.1** (Koopman operator [15]). *For nonlinear dynamic system (2.4), the Koopman operator  $\mathcal{K}^{\mathbf{P}}$  is an infinite-dimensional linear operator that acts on all observable functions  $g : \mathcal{M} \rightarrow \mathbb{C}$  so that*

$$\mathcal{K}^{\mathbf{P}}g(\mathbf{Q}(t; \mathbf{p})) = g(\mathbf{F}(\mathbf{Q}(t; \mathbf{p}); \mathbf{p})). \quad (3.1)$$

*For discrete dynamic system (2.5), the discrete-time Koopman operator  $\mathcal{K}_{\Delta t}^{\mathbf{P}}$  is*

$$\mathcal{K}_{\Delta t}^{\mathbf{P}}g(\mathbf{Q}(t_{k+1}; \mathbf{p})) = g(\mathbf{F}_{\Delta t}(\mathbf{Q}(t_k; \mathbf{p}); \mathbf{p})) = g(\mathbf{Q}(t_{k+1}; \mathbf{p})). \quad (3.2)$$

The Koopman operator transforms the finite-dimensional nonlinear problem (2.4) in the state space into the infinite-dimensional linear problem (3.1) in the observable space. Since  $\mathcal{K}_{\Delta t}^{\mathbf{P}}$  is an infinite-dimensional linear operator, it is equipped with infinite eigenvalues  $\{\lambda_k(\mathbf{p})\}_{k=1}^{\infty}$  and eigenfunctions  $\{\phi_k(\mathbf{p})\}_{k=1}^{\infty}$ . In practice, one has to make a finite approximation of the eigenvalues and eigenfunctions. The following assumption is essential to both a finite-dimensional approximation and the choice of observables.

**Assumption 3.1.** *Let  $\mathbf{y}(t_k; \mathbf{p})$  denote a  $N \times 1$  vector of observables,*

$$\mathbf{y}(t_k; \mathbf{p}) = \mathbf{g}(\mathbf{Q}(t_k; \mathbf{p})) = \begin{bmatrix} g_1(\mathbf{Q}(t_k; \mathbf{p})) \\ \vdots \\ g_N(\mathbf{Q}(t_k; \mathbf{p})) \end{bmatrix}, \quad (3.3)$$

*where  $g_j : \mathcal{M} \rightarrow \mathbb{C}$  is an observable function with  $j = 1, \dots, N$ . If the chosen observable  $\mathbf{g}$  is restricted to an invariant subspace spanned by eigenfunctions of the Koopman operator  $\mathcal{K}_{\Delta t}^{\mathbf{P}}$ , then it induces a linear operator  $\mathbf{K}(\mathbf{p})$  that is finite-dimensional and advances these eigenobservable functions on this subspace [41].*

Based on Assumption 3.1, one can deploy the DMD algorithm 1. to approximate the  $N$ -dimensional linear operator  $\mathbf{K}(\mathbf{p})$  and its low dimensional approximation  $\mathbf{K}_r(\mathbf{p})$  of rank  $r$ . At each parameter point  $\mathbf{p}^{(i)}, i = 1, \dots, N_{\text{MC}}$ , the discrete HFM (2.5) on state space is approximated by a  $N$ -dimensional linear surrogate model

$$\mathbf{y}(t_{k+1}; \mathbf{p}^{(i)}) = \mathbf{K}(\mathbf{p}^{(i)})\mathbf{y}(t_k; \mathbf{p}^{(i)}) \quad (3.4)$$

on observable space. The two spaces are connected by the observable function  $\mathbf{g}$  and its inverse  $\mathbf{g}^{-1}$ . Algorithm 1 induces the following ROM for (3.4) directly,

$$\mathbf{q}(t_{k+1}; \mathbf{p}^{(i)}) = \mathbf{K}_r(\mathbf{p}^{(i)})\mathbf{q}(t_k; \mathbf{p}^{(i)}), \quad (3.5)$$

where

$$\mathbf{y}(t_k; \mathbf{p}^{(i)}) = \mathbf{V}(\mathbf{p}^{(i)})\mathbf{q}(t_k; \mathbf{p}^{(i)}), \quad \mathbf{K}_r(\mathbf{p}^{(i)}) = \mathbf{V}(\mathbf{p}^{(i)})^{\top} \mathbf{K}(\mathbf{p}^{(i)}) \mathbf{V}(\mathbf{p}^{(i)}). \quad (3.6)$$

---

**Algorithm 1:** DMD algorithm on observable space [15] for parameter point  $\mathbf{p}^{(i)}, i = 1, \dots, N_{MC}$ .

---

Input:  $\{\mathbf{Q}(t_0; \mathbf{p}^{(i)}), \dots, \mathbf{Q}(t_{N_{\text{snap}}}; \mathbf{p}^{(i)})\}$ , observable function  $\mathbf{g}$ ,

1. Create the data matrices of observables

$$\mathbf{Y}_1(\mathbf{p}^{(i)}) = \begin{bmatrix} | & & | \\ \mathbf{y}(t_0; \mathbf{p}^{(i)}) & \cdots & \mathbf{y}(t_{N_{\text{snap}}-1}; \mathbf{p}^{(i)}) \\ | & & | \end{bmatrix}, \quad \mathbf{Y}_2(\mathbf{p}^{(i)}) = \begin{bmatrix} | & & | \\ \mathbf{y}(t_1; \mathbf{p}^{(i)}) & \cdots & \mathbf{y}(t_{N_{\text{snap}}}; \mathbf{p}^{(i)}) \\ | & & | \end{bmatrix}, \quad (3.7)$$

where each column is given by  $\mathbf{y}(t_k; \mathbf{p}^{(i)}) = \mathbf{g}(\mathbf{Q}(t_k; \mathbf{p}^{(i)}))$ .

2. Apply SVD  $\mathbf{Y}_1(\mathbf{p}^{(i)}) \approx \mathbf{V}(\mathbf{p}^{(i)})\mathbf{\Sigma}(\mathbf{p}^{(i)})\mathbf{Z}(\mathbf{p}^{(i)})^*$  with  $\mathbf{V}(\mathbf{p}^{(i)}) \in \mathbb{C}^{N \times r}$ ,  $\mathbf{\Sigma}(\mathbf{p}^{(i)}) \in \mathbb{C}^{r \times r}$ ,  $\mathbf{Z}(\mathbf{p}^{(i)}) \in \mathbb{C}^{r \times (N_{\text{snap}}-1)}$ , where  $r$  is the truncated rank chosen by certain criteria and should be the same for all  $i = 1, \dots, N_{MC}$ .
3. Compute  $\mathbf{K}_r(\mathbf{p}^{(i)}) = \mathbf{V}(\mathbf{p}^{(i)})^* \mathbf{Y}_2(\mathbf{p}^{(i)}) \mathbf{Z}(\mathbf{p}^{(i)}) \mathbf{\Sigma}(\mathbf{p}^{(i)})^{-1}$  as an  $r \times r$  low-rank approximation for  $\mathbf{K}(\mathbf{p}^{(i)})$ .
4. Compute  $\mathbf{P}^{(i,j)} = \mathbf{V}(\mathbf{p}^{(i)})^\top \mathbf{V}(\mathbf{p}^{(j)})$  for  $i, j = 1, \dots, N_{MC}$ .

Output:  $\mathbf{V}(\mathbf{p}^{(i)})$ ,  $\mathbf{K}_r(\mathbf{p}^{(i)})$  and  $\mathbf{P}^{(i,j)}$ .

---

**Remark 3.1.** Notice that the above step can be done offline.  $\mathbf{P}^{(i,j)}$  are precomputed for the later online step. Although the offline step takes a majority of the computational costs in the whole framework mostly due to the computation for the high-fidelity training data (2.6), the output of this step can be pre-computed and stored efficiently (the output storage is  $(N \times r + r \times r + r \times r \times \frac{N_{MC}+1}{2}) \times N_{MC}$ ). In practice, real-time applications can be enabled as long as the online step is sufficient enough.

**Remark 3.2.** Connections between the DMD theory and the Koopman spectral analysis under specific conditions on the observables and collected data are established by a theorem in [42]. This theorem indicates that judicious selection of the observables is critical to success of the Koopman method. In general, there is no principled way to select observables without expert knowledge of a dynamical system. Machine learning techniques can be deployed to identify relevant terms in the dynamics from data, which guide selection of the observables [43, 44, 44]. In our numerical examples, we select the observables based on knowledge about the underlying physics (similar to previous works [21, 22, 23, 24, 45, 46]).

### 3.2. Online Step: Interpolation of ROBs and PROMs

For an unsampled parameter point  $\mathbf{p}^* \notin \{\mathbf{p}^{(1)}, \dots, \mathbf{p}^{(N_{MC})}\}$ , the goal is to compute  $\{\mathbf{Q}(t_1; \mathbf{p}^*), \dots, \mathbf{Q}(t_{N_T}; \mathbf{p}^*)\}$  via the following PROM without computing the complex high dimensional system (2.2) and (2.3):

$$\mathbf{q}(t_{k+1}; \mathbf{p}^*) = \mathbf{K}_r(\mathbf{p}^*) \mathbf{q}(t_k; \mathbf{p}^*). \quad (3.8)$$

Subsequently, the state variable can be computed by

$$\mathbf{y}(t_k; \mathbf{p}^*) = \mathbf{V}(\mathbf{p}^*)\mathbf{q}(t_k; \mathbf{p}^*), \quad \mathbf{Q}(t_k; \mathbf{p}^*) = \mathbf{g}^{-1}(\mathbf{y}(t_k; \mathbf{p}^*)). \quad (3.9)$$

Therefore, the online task includes 1. Computing  $\mathbf{V}(\mathbf{p}^*)$ ; 2. Computing  $\mathbf{K}_r(\mathbf{p}^*)$ ; 3. Computing  $\mathbf{q}(t_k; \mathbf{p}^*)$ .

### 3.2.1. Interpolating ROBs

In order to compute the ROB  $\mathbf{V}(\mathbf{p}^*)$  needed in (3.9), the following interpolation on Grassman manifold is made from  $\{\mathbf{V}(\mathbf{p}^{(1)}), \dots, \mathbf{V}(\mathbf{p}^{(N_{\text{MC}})})\}$ . Here we briefly review the interpolation approach proposed in [33].

**Definition 3.2.** *First we denote the following matrix manifold of interest:*

- *Grassmann manifold  $\mathcal{G}(r, N)$  is the set of all subspaces in  $\mathbb{R}^N$  of dimension  $r$ ;*
- *Orthogonal Stiefel Manifold  $\mathcal{ST}(r, N)$  is the set of orthogonal ROB matrices in  $\mathbb{R}^{r \times N}$ .*

Recall that  $\mathbf{V}(\mathbf{p}^{(i)}) \in \mathbb{R}^{N \times r}, i = 1, \dots, N_{\text{MC}}$ , where  $r \leq N$ , denote the full-rank column matrix, whose columns provide a basis of subspace  $\mathcal{S}_i$  of dimension  $r$  in  $\mathbb{R}^N$ . The associated ROM is not uniquely defined by the ROB but uniquely defined by the subspace  $\mathcal{S}_i$ . Therefore, the correct entity to interpolate is the subspaces  $\mathcal{S}_i$  instead of the ROB  $\mathbf{V}(\mathbf{p}^{(i)})$ . The goal is now shifted to compute  $\mathcal{S}_* = \text{range}(\mathbf{V}(\mathbf{p}^*))$  by interpolating  $\{\mathcal{S}_i\}_{i=1}^{N_{\text{MC}}}$  with access to a ROB  $\mathbf{V}(\mathbf{p}^*)$ .

The subspaces  $\mathcal{S}_i$  belongs to the Grassmann manifold [47, 48, 49, 50, 51]  $\mathcal{G}(r, N)$ . Each  $r$ -dimensional subspace  $\tilde{\mathcal{S}}$  of  $\mathbb{R}^N$  can be regarded as a point of  $\mathcal{G}(r, N)$  and nonuniquely represented by a matrix  $\tilde{\mathbf{V}} \in \mathbb{R}^{N \times r}$  whose columns span the subspace  $\tilde{\mathcal{S}}$ . The matrices  $\tilde{\mathbf{V}}$  are chosen among those whose columns form a set of orthonormal vectors of  $\mathbb{R}^N$  and belong to the orthogonal Stiefel manifold  $\mathcal{ST}(r, N)$  [47, 51]. There exists a projection map [47] from  $\mathcal{ST}(r, N)$  to  $\mathcal{G}(r, N)$ , as each matrix in  $\mathcal{ST}(r, N)$  spans a subspace of  $\mathbb{R}^N$  of dimension  $r$  and different matrices can span the same subspace. At each point  $\tilde{\mathcal{S}}$  of the manifold  $\mathcal{G}(r, N)$ , there exists a tangent space [47, 51] of the same dimension [51]. This space is denoted by  $\mathcal{T}_{\tilde{\mathcal{S}}}$  and each of its points can be represented by a matrix  $\tilde{\mathbf{\Gamma}} \in \mathbb{R}^{N \times r}$ . This tangent space is a vector space where usual interpolation is allowed for the matrices representing points of  $\mathcal{T}_{\tilde{\mathcal{S}}}$ . Let  $\mathbf{\Gamma}^i = m_{\mathbf{V}}(\mathbf{V}(\mathbf{p}^{(i)}))$ , where  $m_{\mathbf{V}}$  denote the map from the matrix manifolds  $\mathcal{G}(r, N)$  to the tangent space. Then the goal is to compute  $\mathbf{\Gamma}^*$  by performing usual interpolation on  $\{\mathbf{\Gamma}^i\}_{i=1}^{N_{\text{MC}}}$  and get back to  $\mathbf{V}(\mathbf{p}^*)$  through the inverse map  $m_{\mathbf{V}}^{-1}(\mathbf{\Gamma}^*)$ .

$m_{\mathbf{V}}$  is chosen to be the logarithm mapping (which maps the Grassmann manifold to its tangent space), and  $m_{\mathbf{V}}^{-1}$  is chosen to be the exponential mapping (which maps the tangent space to the Grassmann manifold itself). This choice borrows concepts of geodesic path on a Grassmann manifold from differential

geometry [47, 48, 52, 53]. We summarize the algorithm as follows and refer the readers to [33] for the detailed construction.

---

**Algorithm 2:** Interpolation of ROBs [33]

---

Input:  $\{\mathbf{V}(\mathbf{p}^{(i)})\}_{i=1}^{N_{\text{MC}}}$ ,  $\{\mathbf{P}^{(i,j)}\}_{i,j=1}^{N_{\text{MC}}}$ ,  $\{\mathbf{p}^{(i)}\}_{i=1}^{N_{\text{MC}}}$  and target parameter point  $\mathbf{p}^*$ ,

1. Denote  $\mathcal{S}_i = \text{range}(\mathbf{V}(\mathbf{p}^{(i)}))$ ,  $i = 1, \dots, N_{\text{MC}}$ . A point  $\mathcal{S}_{i_0}, i_0 \in \{1, \dots, N_{\text{MC}}\}$  of the manifold is chosen as a reference and origin point for interpolation;
2. Select the points  $\mathcal{S}_i, i \in \mathcal{I}_{i_0} \subset \{1, \dots, N_{\text{MC}}\}$  which lie in a sufficiently small neighborhood of  $\mathcal{S}_{i_0}$  and map those  $\{\mathcal{S}_i\}_{i \in \mathcal{I}_{i_0}}$  to matrices  $\{\mathbf{\Gamma}^i\}_{i \in \mathcal{I}_{i_0}}$  representing corresponding points of  $\mathcal{T}_{\mathcal{S}_{i_0}}$  using the logarithm map  $\log_{\mathcal{S}_{i_0}}$ . This can be computed by

$$\begin{aligned} (\mathbf{I} - \mathbf{V}(\mathbf{p}^{(i_0)})\mathbf{V}(\mathbf{p}^{(i_0)})^\top)\mathbf{V}(\mathbf{p}^{(i)})(\mathbf{P}^{(i_0,i)})^{-1} &= \mathbf{U}_i\mathbf{\Omega}_i\mathbf{W}_i^\top, \quad (\text{thin SVD}) \\ \mathbf{\Gamma}^i &= \mathbf{U}_i \tan^{-1}(\mathbf{\Omega}_i)\mathbf{W}_i^\top. \end{aligned} \quad (3.10)$$

3. Compute  $\mathbf{\Gamma}^*$  by interpolating  $\{\mathbf{\Gamma}^i\}_{i \in \mathcal{I}_{i_0}}$  entry by entry:

$$\mathbf{\Gamma}_{ij}^* = \mathcal{P}(\mathbf{p}^*; \{\mathbf{\Gamma}_{ij}^i, \mathbf{p}^{(i)}\}_{i \in \mathcal{I}_{i_0}}), \quad i = 1, \dots, N, \quad j = 1, \dots, r. \quad (3.11)$$

4. Map the matrix  $\mathbf{\Gamma}^*$  representing a point of  $\mathcal{T}_{\mathcal{S}_{i_0}}$  to the desired subspace  $\mathcal{S}_*$  on  $\mathcal{G}(r, N)$  spanned by a ROB  $\mathbf{V}(\mathbf{p}^*)$  using the exponential map  $\exp_{\mathcal{S}_{i_0}}$ . This can be computed by

$$\begin{aligned} \mathbf{\Gamma}^* &= \mathbf{U}_* \tan^{-1}(\mathbf{\Omega}_*)\mathbf{W}_*^\top, \quad (\text{thin SVD}) \\ \mathbf{V}(\mathbf{p}^*) &= \mathbf{V}(\mathbf{p}^{(i_0)})\mathbf{W}_* \cos(\mathbf{\Omega}_*) + \mathbf{U}_* \sin(\mathbf{\Omega}_*) \end{aligned} \quad (3.12)$$

Output:  $\mathbf{V}(\mathbf{p}^*)$ .

---

**Remark 3.3.** The choice of the interpolation method  $\mathcal{P}$  depends on the dimension of the parameter  $N_{\text{par}}$ . When  $N_{\text{par}} = 1$ , a univariate (typically, a Lagrange type) interpolation method is chosen. Otherwise, a multivariate interpolation scheme (see, for example, [54, 55]) is chosen.

**Remark 3.4.** Because the logarithmic map  $\log_{\mathcal{S}_{i_0}}$  is defined in a neighborhood of  $\mathcal{S}_{i_0} \in \mathcal{G}(r, N)$ , the method is not sensitive, in principle, to the choice of the reference point  $\mathcal{S}_{i_0}$  in step 1 of Algorithm 2. This is also confirmed in practice [33].

### 3.2.2. Interpolating PROMs

In order to compute the reduced order operator  $\mathbf{K}_r(\mathbf{p}^*)$  needed in (3.8), the following interpolation on matrix manifold is made from ROMs  $\{\mathbf{K}_r(\mathbf{p}^{(1)}), \dots, \mathbf{K}_r(\mathbf{p}^{(N_{\text{MC}})})\}$ . We briefly review the approach proposed in [34] consisting of the following two steps:

- Step A). As discussed before, a given ROM can be expressed in a variety of equivalent ROBs. The resulting ROMs may not have been precomputed in the same generalized coordinates system.



The validity of an interpolation may crucially depend on the choice of the representative element within each equivalent class. Given the precomputed ROMs  $\{\mathbf{K}_r(\mathbf{p}^{(1)}), \dots, \mathbf{K}_r(\mathbf{p}^{(N_{\text{MC}})})\}$ , a set of congruence transformations is determined so that a representative element of the equivalent ROB for each precomputed ROM is chosen to align the precomputed ROMs into consistent sets of generalized coordinates. The consistency can be enforced by solving the following classical orthogonal Procrustes problems [56]:

$$\min_{\mathbf{Q}_i, \mathbf{Q}_i^\top \mathbf{Q}_i = \mathbf{I}_r} \|\mathbf{V}(\mathbf{p}^{(i)})^\top \mathbf{Q}_i - \mathbf{V}(\mathbf{p}^{(i_0)})\|_F, \forall i = 1, \dots, N_{\text{MC}}, \quad (3.13)$$

where  $i_0 \in \{1, \dots, N_{\text{MC}}\}$  is chosen as a reference configuration. The representative element can be identified by solving the above problem analytically. We summarize the algorithm below and refer the readers to [34] for details.

---

**Algorithm 3:** Step A of interpolating PROMs [33]

---

Input:  $\{\mathbf{K}_r(\mathbf{p}^{(1)}), \dots, \mathbf{K}_r(\mathbf{p}^{(N_{\text{MC}})})\}$ ,  $\{\mathbf{P}^{(i,j)}\}_{i,j=1}^{N_{\text{MC}}}$ , reference configuration choice  $i_0$ ,

**For**  $i \in \{1, \dots, N_{\text{MC}}\} \setminus \{i_0\}$

- Compute  $\mathbf{P}^{(i,i_0)} = \mathbf{U}_{i,i_0} \boldsymbol{\Sigma}_{i,i_0} \mathbf{Z}_{i,i_0}^\top$  (SVD),
- Compute  $\mathbf{Q}_i = \mathbf{U}_{i,i_0} \mathbf{Z}_{i,i_0}^\top$ ,
- Transform  $\tilde{\mathbf{K}}_r(\mathbf{p}^{(i)}) = \mathbf{Q}_i^\top \mathbf{K}_r(\mathbf{p}^{(i)}) \mathbf{Q}_i$

**End**

Output:  $\{\tilde{\mathbf{K}}_r(\mathbf{p}^{(1)}), \dots, \tilde{\mathbf{K}}_r(\mathbf{p}^{(N_{\text{MC}})})\}$ .

---

**Remark 3.5.** An optimal choice of the reference configuration  $i_0$ , if it exists, remains an open problem.

**Remark 3.6.** The above step A is related to mode tracking procedures based on the modal assurance criterion (MAC) [57]. The connection is illustrated in [34].

- Step B). The transformed ROMs  $\{\tilde{\mathbf{K}}_r(\mathbf{p}^{(1)}), \dots, \tilde{\mathbf{K}}_r(\mathbf{p}^{(N_{\text{MC}})})\}$  are interpolated to compute a ROM  $\mathbf{K}_r(\mathbf{p}^*)$ . Similar to section 3.2.1, this interpolation must be performed on a specific manifold containing  $\{\tilde{\mathbf{K}}_r(\mathbf{p}^{(1)}), \dots, \tilde{\mathbf{K}}_r(\mathbf{p}^{(N_{\text{MC}})})\}$  and  $\mathbf{K}_r(\mathbf{p}^*)$  so that the distinctive properties (e.g., orthogonality, nonsingularity) can be preserved. The main idea again is to first map all precomputed matrices to the tangent space to the matrix manifold of interest at a chosen reference point using the logarithm mapping, interpolate the mapped data in this linear vector space, and finally map the interpolated result back to the manifold of interest using the associated exponential map. The

algorithm is described as follows:

---

**Algorithm 4:** Step B of interpolating PROMs [33]

---

Input:  $\{\tilde{\mathbf{K}}_r(\mathbf{p}^{(1)}), \dots, \tilde{\mathbf{K}}_r(\mathbf{p}^{(N_{\text{MC}})})\}$ , reference configuration choice  $i_0$ ,

1. **For**  $i \in \{1, \dots, N_{\text{MC}}\} \setminus \{i_0\}$

– Compute  $\mathbf{\Gamma}^i = \log_{\tilde{\mathbf{K}}_r(\mathbf{p}^{(i_0)})}(\tilde{\mathbf{K}}_r(\mathbf{p}^{(i)}))$ ,

**End**

2. Compute  $\mathbf{\Gamma}^*$  by interpolating  $\{\mathbf{\Gamma}^i\}_{i \in \mathcal{I}_{i_0}}$  entry by entry the same as (3.11).

3. Compute  $\mathbf{K}_r(\mathbf{p}^*) = \exp_{\tilde{\mathbf{K}}_r(\mathbf{p}^{(i_0)})}(\mathbf{\Gamma}^*)$ .

Output:  $\mathbf{K}_r(\mathbf{p}^*)$ .

---

**Remark 3.7.** The log and exp denote the matrix logarithm and exponential respectively. The specific expressions of different matrix manifolds of interest are listed in Table 4.1 of [34].

### 3.2.3. Iteration-free Computation of the Solution

With  $\mathbf{K}_r(\mathbf{p}^*)$  and  $\mathbf{V}(\mathbf{p}^*)$ , one can compute the solution using the iteration-free feature of DMD framework. The algorithm is summarized as below:

---

**Algorithm 5:** DMD Reconstruction

---

Input:  $\mathbf{K}_r(\mathbf{p}^*)$ ,  $\mathbf{V}(\mathbf{p}^*)$ ,  $\mathbf{y}(t=0; \mathbf{p}^*)$ ,  $\mathbf{g}$ .

1. Compute the eigen-decomposition of  $\mathbf{K}_r(\mathbf{p}^*)$ :

$$\mathbf{K}_r(\mathbf{p}^*)\mathbf{\Psi}(\mathbf{p}^*) = \mathbf{\Psi}(\mathbf{p}^*)\mathbf{\Lambda}(\mathbf{p}^*), \quad (3.14)$$

where columns of  $\mathbf{\Psi}(\mathbf{p}^*)$  are eigenvectors and  $\mathbf{\Lambda}(\mathbf{p}^*)$  is a diagonal matrix containing the corresponding eigenvalues  $\lambda_i, i = 1, \dots, r$ .

2. Compute the DMD modes

$$\mathbf{\Phi}(\mathbf{p}^*) = \mathbf{V}(\mathbf{p}^*)\mathbf{\Psi}(\mathbf{p}^*). \quad (3.15)$$

3. Reconstruct the observables:

$$\mathbf{y}_{\text{DMD}}(t_k; \mathbf{p}^*) = \mathbf{\Phi}(\mathbf{p}^*)\mathbf{\Lambda}(\mathbf{p}^*)^k (\mathbf{\Phi}(\mathbf{p}^*)^{-1}\mathbf{y}(0; \mathbf{p}^*)), k = 1, \dots, N_T. \quad (3.16)$$

4. Map the observables back to state space:

$$\mathbf{Q}_{\text{DMD}}(t_k; \mathbf{p}^*) = \mathbf{g}^{-1}(\mathbf{y}_{\text{DMD}}(t_k; \mathbf{p}^*)). \quad (3.17)$$

Output:  $\mathbf{Q}_{\text{DMD}}(t_k; \mathbf{p}^*)$ .

---

### 3.3. Algorithm Summary

The proposed DMD-PROM framework is summarized below:

---

**Algorithm 6:** DMD-PROM framework

---

*Offline Step:*

**For**  $i = 1, \dots, N_{\text{MC}}$ ,

    Compute the high fidelity training data (2.6),

    Input:  $\{\mathbf{Q}(t_1; \mathbf{p}^{(i)}), \dots, \mathbf{Q}(t_{N_{\text{snap}}}; \mathbf{p}^{(i)})\}$  and  $\mathbf{g} \xrightarrow{\text{Algorithm 1}}$  Output:  $\mathbf{V}(\mathbf{p}^{(i)}), \mathbf{K}_r(\mathbf{p}^{(i)})$  and  $\mathbf{P}^{(i,j)}$

**End**

*Online Step:*

- Interpolation of ROBs:

    Input:  $\{\mathbf{V}(\mathbf{p}^{(i)})\}_{i=1}^{N_{\text{MC}}}, \{\mathbf{P}^{(i,j)}\}_{i,j=1}^{N_{\text{MC}}}, \{\mathbf{p}^{(i)}\}_{i=1}^{N_{\text{MC}}}, \mathbf{p}^* \xrightarrow{\text{Algorithm 2}}$  Output:  $\mathbf{V}(\mathbf{p}^*)$

- Interpolation of PROMs:

    Input:  $\{\mathbf{K}_r(\mathbf{p}^{(i)})\}_{i=1}^{N_{\text{MC}}}, \{\mathbf{P}^{(i,j)}\}_{i,j=1}^{N_{\text{MC}}}$ , reference choice  $i_0 \xrightarrow{\text{Algorithm 3\& 4}}$  Output:  $\mathbf{K}_r(\mathbf{p}^*)$

- DMD reconstruction:

    Input:  $\mathbf{K}_r(\mathbf{p}^*), \mathbf{V}(\mathbf{p}^*), \mathbf{y}(t=0; \mathbf{p}^*), \mathbf{g} \xrightarrow{\text{Algorithm 5}}$  Output:  $\mathbf{Q}_{\text{DMD}}(t_k; \mathbf{p}^*)$

---

**Remark 3.8.** The sampling strategy for  $\{\mathbf{p}^{(1)}, \dots, \mathbf{p}^{(N_{\text{MC}})}\}$  in the parameter space plays a key role in the accuracy of the subspace approximation. The so-called ‘‘curse of dimensionality’’, i.e., the number of training samples  $N_{\text{MC}}$  needed grows exponentially with the dimension of the parameter  $N_{\text{par}}$ , is a well-known challenge. In general, uniform sampling is used for  $N_{\text{par}} \leq 5$  and moderately computationally intensive HFMs, latin hypercube sampling is used for  $N_{\text{par}} > 5$  and moderately computationally intensive HFMs, and adaptive, goal-oriented, greedy sampling is used for  $N_{\text{par}} > 5$  and highly computationally intensive HFMs. In the following numerical examples, we demonstrate our framework with  $N_{\text{par}} = 1$  for simplicity. The challenge for higher dimensions is considered as out of the scope of this work and will be studied for future work.

## 4. Numerical Tests

### 4.1. POD-PROM vs. DMD-PROM

Consider a two-dimensional advection-diffusion equation

$$\frac{\partial s}{\partial t} + \mathbf{U} \cdot \nabla s - \kappa \Delta s = 0, \text{ for } \mathbf{x} = (x, y) \in [0, 1] \times [0, 1], t \in [0, 1], \quad (4.1)$$

with the boundary conditions

$$\begin{aligned} s(\mathbf{x}; p) &= s_D(y, t), \text{ for } \mathbf{x} = (x, y) \in \Gamma_D = \{0\} \times [0, 1] \\ \nabla s(\mathbf{x}; p) \cdot \mathbf{n}(\mathbf{x}) &= 0, \text{ for } \mathbf{x} \in \Gamma_N = \{\{1\} \times [0, 1]\} \cup \{[0, 1] \times \{1\}\} \cup \{[0, 1] \times \{0\}\} \end{aligned} \quad (4.2)$$

where

$$s_D(y, t) = \begin{cases} 300 & \text{if } y \in [0, \frac{1}{3}] \\ 300 + 325(\sin(3\pi|y - \bar{y}|) + 1) & \text{if } y \in [\frac{1}{3}, \frac{2}{3}] \\ 300 & \text{if } y \in [\frac{2}{3}, 1] \end{cases} \quad (4.3)$$

and  $\mathcal{U} = \begin{bmatrix} \mathcal{U}_1 \\ \mathcal{U}_2 \end{bmatrix}$ , with  $\mathcal{U}_1 = p \in [0, 5000]$  and  $\mathcal{U}_2 = 0$ ,  $\kappa = 250$ ,  $\bar{y} = 0.4$ .

The high fidelity solution is obtained via discretizing the above problem by finite differences using 75 points in each spatial direction. Then the fully discretized variable  $\mathbf{S}(t; p)$  is of high dimension  $N_{sv} = 75^2$ . Using upwind scheme for the advection term and implicit center difference scheme for the diffusion term with  $\Delta t = 0.01$ , the QoIs are chosen as  $\mathbf{Q}(t^n; p) = \mathbf{S}(t^n; p)$ , which follows the high fidelity linear model:

$$\mathbf{Q}(t^{n+1}; p) = \mathbf{A}(p)\mathbf{Q}(t^n; p) + \mathbf{b}(p). \quad (4.4)$$

The training data is generated from the high fidelity simulation (4.4) on parameter samples  $p^{(1)} = 1000$  and  $p^{(2)} = 4000$ . The trajectories of the solution on these two parameter samples are shown on the first two rows of Figure 1. The goal is to obtain the solution on the target parameter point  $p^* = 2000$  without computing (4.4). A reference solution  $\mathbf{Q}(t; p^*)$  on the target parameter point computed by the high fidelity simulation (4.4) is shown on the bottom row of Figure 1 as a reference.

We compare the performances of POD-PROM (Algorithm S1) and DMD-PROM (Algorithm 6) in this problem. Notice that the main difference of the two methods is the way to compute the ROM  $(\mathbf{A}_r(p^{(i)}), \mathbf{b}_r(p^{(i)}))$  and  $\mathbf{K}_r(p^{(i)})$  in the offline step. In POD-PROM,  $(\mathbf{A}_r(p^{(i)}), \mathbf{b}_r(p^{(i)}))$  are obtained from the Galerkin projection (S1) (or alternative projections, e.g., Petrov-Galerkin, DEIM, etc.), which requires the full knowledge of  $\mathbf{A}(p^{(i)})$  and  $\mathbf{b}(p^{(i)})$ . However, such requirements are lifted in DMD-PROM as  $\mathbf{K}_r(p^{(i)})$  are learned from the training dataset (2.6). In this linear case, one can set the observable function  $\mathbf{g}$  as

$$\mathbf{y} = \mathbf{g}(\mathbf{Q}) = [1, \mathbf{Q}^\top]^\top, \quad (4.5)$$

then the observable  $\mathbf{y}$  essentially follows the following equation

$$\mathbf{y}(t^{n+1}; p) = \mathbf{K}(p)\mathbf{y}(t^n; p), \quad \mathbf{K}(p) = \begin{bmatrix} 1 & 0 \\ \mathbf{b}(p) & \mathbf{A}(p) \end{bmatrix}. \quad (4.6)$$

Alternatively, one can use xDMD proposed in [24] for the offline step.

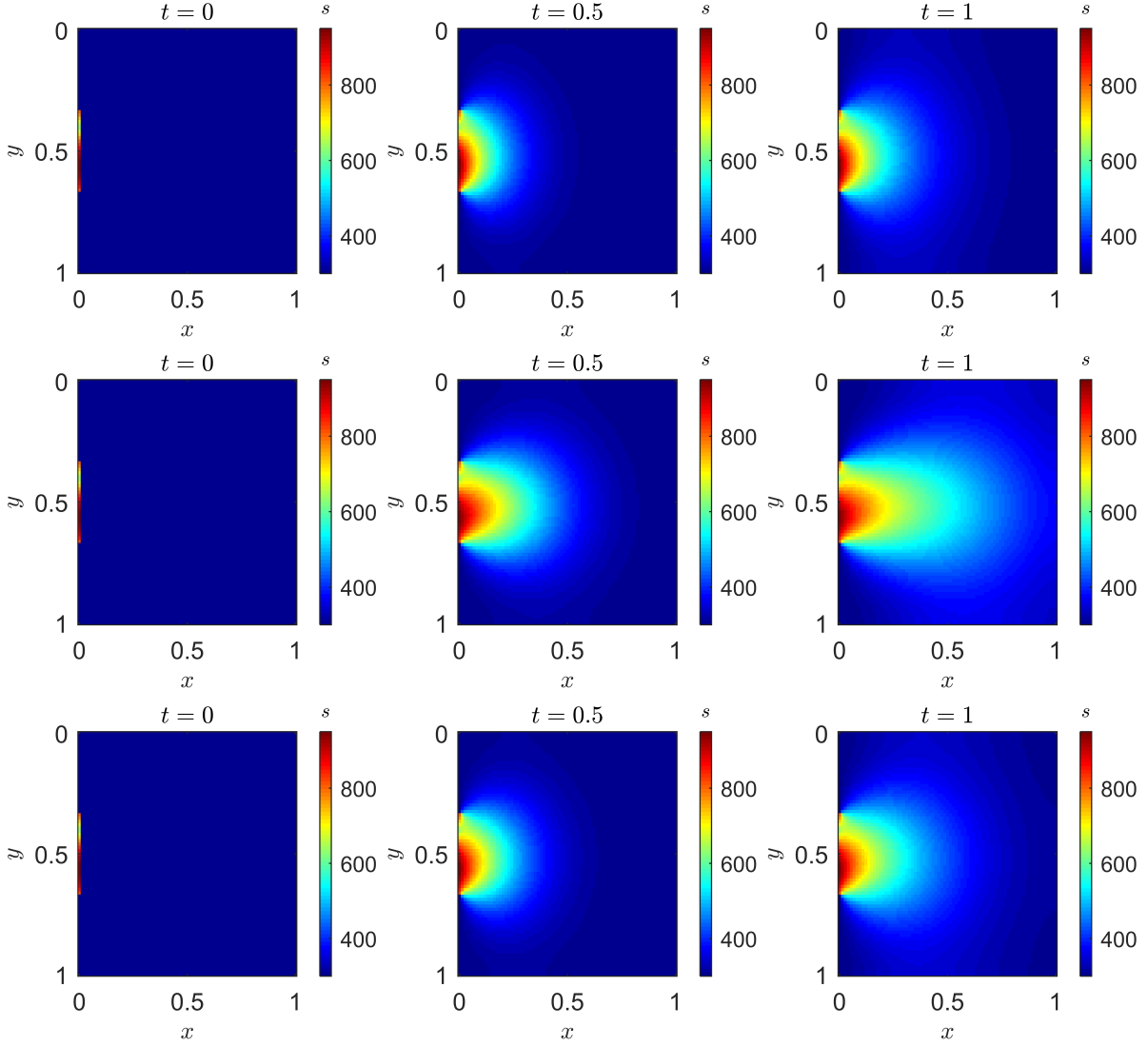


Figure 1: Top row: training data from the parameter sample point  $p^{(1)} = 1000$ ; Middle row: training data from the parameter sample point  $p^{(2)} = 4000$ ; Bottom row: reference solution of the test data from the parameter sample point  $p^* = 2000$ . All is generated via the high fidelity simulation (4.4).

Define the relative  $L_2$  errors of the POD-PROM and DMD-PROM compared to the reference HFM at the test parameter point  $p^*$  as

$$\begin{aligned}
 e_{\text{POD}}(t; p^*) &= \frac{\|\mathbf{Q}_{\text{POD}}(t; p^*) - \mathbf{Q}(t; p^*)\|_2}{\|\mathbf{Q}(t; p^*)\|_2}, \\
 e_{\text{DMD}}(t; p^*) &= \frac{\|\mathbf{Q}_{\text{DMD}}(t; p^*) - \mathbf{Q}(t; p^*)\|_2}{\|\mathbf{Q}(t; p^*)\|_2}.
 \end{aligned} \tag{4.7}$$

We construct rank  $r = 10$  POD-PROMs and DMD-PROMs using different numbers of snapshots  $N_{\text{snap}}$ . The relative  $L_2$  error of each are displayed in the left plots of Figure 2. For both methods, the magnitudes of the errors decrease with larger number of  $N_{\text{snap}}$ . In POD, this can be explained by the fact

that the low dimensional subspace (represented by the ROB's determined by the training data) becomes more optimal with larger number of informative data. The same reason holds for DMD. Furthermore, one can observe that DMD has larger error than POD in the case  $N_{\text{snap}} = 25$  and  $N_{\text{snap}} = 50$ . The difference is caused by the loss of accuracy in learning  $\mathbf{K}_r(p^{(i)})$  from data in the DMD framework. Given enough data (in the case  $N_{\text{snap}} = 100$ ), the difference between POD and DMD saturates as the learned  $\mathbf{K}_r(p^{(i)})$  becomes accurate enough.

Define the total relative  $L_2$  errors of the POD-PROM and DMD-PROM as

$$E_{\text{POD}}(p^*) = \frac{\sqrt{\sum_{k=1}^{N_T} \|\mathbf{Q}_{\text{POD}}(t_k; p^*) - \mathbf{Q}(t_k; p^*)\|_2^2}}{\sqrt{\sum_{k=1}^{N_T} \|\mathbf{Q}(t_k; p^*)\|_2^2}},$$

$$E_{\text{DMD}}(p^*) = \frac{\sqrt{\sum_{k=1}^{N_T} \|\mathbf{Q}_{\text{DMD}}(t_k; p^*) - \mathbf{Q}(t_k; p^*)\|_2^2}}{\sqrt{\sum_{k=1}^{N_T} \|\mathbf{Q}(t_k; p^*)\|_2^2}}.$$
(4.8)

We construct POD-PROMs and DMD-PROMs of different ranks  $r$  using the same number of snapshots  $N_{\text{snap}} = N_T = 100$ . The total relative  $L_2$  error of each are displayed in the right plots of Figure 2. Both methods have decreased errors with larger rank  $r$  and the errors saturate after  $r = 10$ , which verifies the low rank nature of this problem. DMD has slightly larger error than POD for small ranks because of the loss in accuracy of learning  $\mathbf{K}_r(p^{(i)})$ . The accuracy of the DMD-based ROM is affected by the number of snapshots and the rank truncation, as studied by many previous papers, e.g., [22].

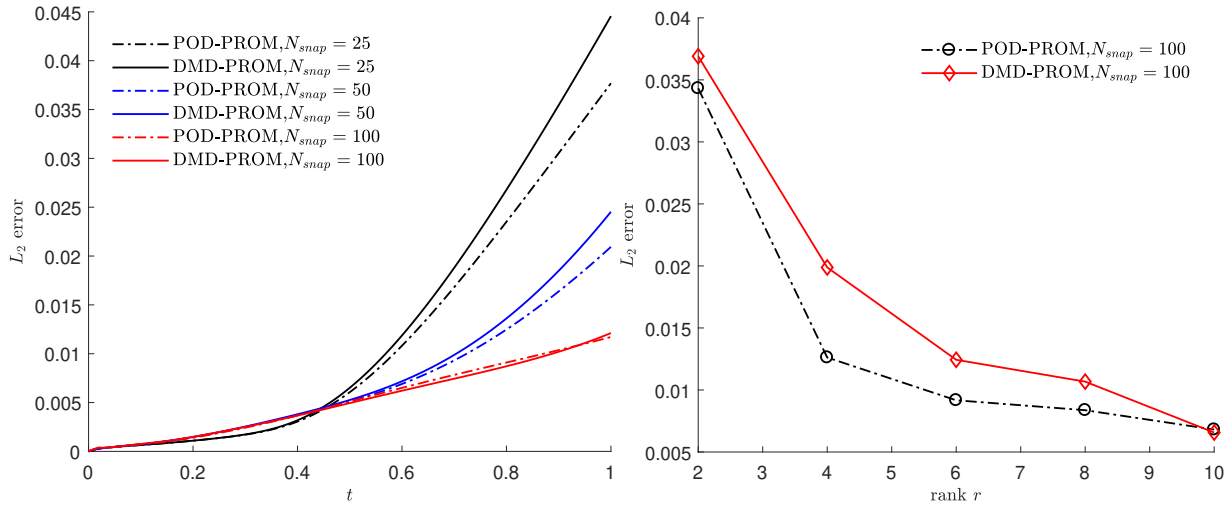


Figure 2: Left: relative  $L_2$  error (4.7) of POD-PROMs and DMD-PROMs using different numbers of snapshots  $N_{\text{snap}}$ ; Right: total relative  $L_2$  error (4.8) of POD-PROMs and DMD-PROMs using different truncated rank  $r$ .

The study of this example illustrates that the knowledge of the physics (i.e., the specific value of  $\mathbf{A}(p^{(i)})$  and  $\mathbf{b}(p^{(i)})$ ) is a privilege in constructing more accurate ROMs (as conventionally done in POD). However, one can still construct satisfactory ROMs without full knowledge of the physics as long as

enough data is given. Our proposed DMD-PROM framework compensates the short of knowledge of the physics by a data-driven learning. The data-driven learning part can be improved by partial knowledge of the physics via the observable function  $\mathbf{g}$ , which has been demonstrated in many previous studies [22, 21, 23, 24, 20, 58]. The following numerical examples will show how to incorporate the physics ingredients into the framework.

#### 4.2. Linear Diffusion Equation

Consider a two-dimensional diffusion equation in a multi-connected domain  $\mathcal{D}$  with inhomogeneous boundary conditions,

$$\begin{cases} \rho c \frac{\partial s}{\partial t} - \nabla \cdot (k \nabla s) = 0, & (x, y) \in \mathcal{D}, \quad t \in (0, 5000]; \quad \rho = 1, k = 1, c = p \in [1, 2]; \\ s(x, y, 0) = 0; \\ s(0, y, t) = 2, \quad s(800, y, t) = 1, \quad \frac{\partial s}{\partial y}(x, 0, t) = \frac{\partial s}{\partial y}(x, 800, t) = 0, \quad s(x, y, t) = 3 \quad \text{on } \partial S \text{ (red)}. \end{cases} \quad (4.9)$$

The domain  $\mathcal{D}$  is the  $800 \times 800$  square with an S-shaped cavity (Figure 3). The Dirichlet boundary conditions are imposed on the left and right sides of the square and the cavity surface. The top and bottom of the square are impermeable. The training data and reference solutions are obtained via Matlab PDE toolbox on the finite-element mesh with 4287 elements shown in Figure 3.

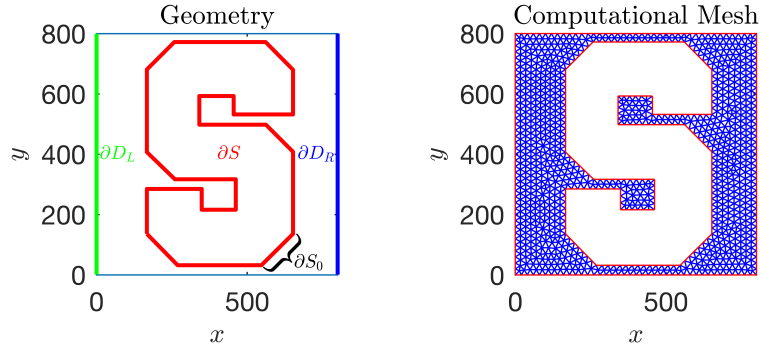


Figure 3: Multi-connected simulation domain  $\mathcal{D}$  (left) and the mesh used in the finite-element solution of (4.9).

First, we consider the case where the QoIs are chosen as  $\mathbf{Q}(t^n; p) = \mathbf{S}(t^n; p)$ . The observable function  $\mathbf{g}$  is chosen the same as (4.5). The training data is generated on the parameter samples  $p^{(1)} = 1$  and  $p^{(2)} = 2$  and the reference solution of a particular test parameter point  $p^* = 1.5$ , together with the absolute error map of the DMD-PROM, are presented in Figure 4. Without the explicit formula of the HFM, which is designed in the Matlab PDE toolbox, our framework can provide an accurate ROM with small rank  $r = 10$ . The Matlab PDE toolbox essentially generates the numerical solutions by solving a HFM iteration in a form of (4.4). If POD framework is used instead, one has to know the exact values

of  $\mathbf{A}(p)$  and  $\mathbf{b}(p)$ , which require large numerical differential matrices and embeddings of the complex boundary conditions. The left plot of Figure 5 shows the accuracy of the 10 rank DMD-PROM for different values of  $p^* \in [1, 2]$ . The error plot has a peak in the middle of the parameter space and decays to its minimum at the two ends, where the errors only come from the differences between the HFMs and the ROMs constructed by local ROBs (at  $p^{(1)} = 1$  and  $p^{(2)} = 2$  respectively).

Then we consider the case where the QoIs are chosen as the heat flux, i.e.,  $\mathbf{Q}_1(t^n; p) = -k\partial_x \mathbf{S}(t^n; p)$  and  $\mathbf{Q}_2(t^n; p) = -k\partial_y \mathbf{S}(t^n; p)$ . The heat flux vector fields of the training data and test reference solutions are plotted using arrows in Figure 4. The observable function  $\mathbf{g}$  is chosen as

$$\mathbf{y} = \mathbf{g}(\mathbf{Q}_1, \mathbf{Q}_2) = [1, \mathbf{Q}_1^\top, \mathbf{Q}_2^\top]^\top. \quad (4.10)$$

The middle plot of Figure 5 shows the accuracy of the 20 rank DMD-PROM for different values of  $p^* \in [1, 2]$ . Similar error distributions are observed as before.

Finally, we consider the case where the QoIs are chosen as the heat rate across the edge of interest (shown in Figure 3), i.e.,  $Q(t^n; p) = \int_{\partial S_0} -k\nabla s(t^n, \mathbf{x}; p) \cdot \vec{\mathbf{n}}_{\partial S_0} dA$ . The observable function  $\mathbf{g}$  is chosen as Hermite polynomials  $\mathcal{H}$  of  $Q(t^n; p)$  up to order  $m = 8$ ,

$$\mathbf{y} = \mathbf{g}(Q) = [\mathcal{H}_0(Q), \dots, \mathcal{H}_{m-1}(Q)]^\top. \quad (4.11)$$

The right plot of Figure 5 shows the accuracy of the 8 rank DMD-PROM for different values of  $p^* \in [1, 2]$ . Similar error distributions are observed as before. The data-driven learning ability of the DMD allows one to construct the ROM for the QoIs directly without accessing the expensive HFM and post-processing the high dimensional state variables.



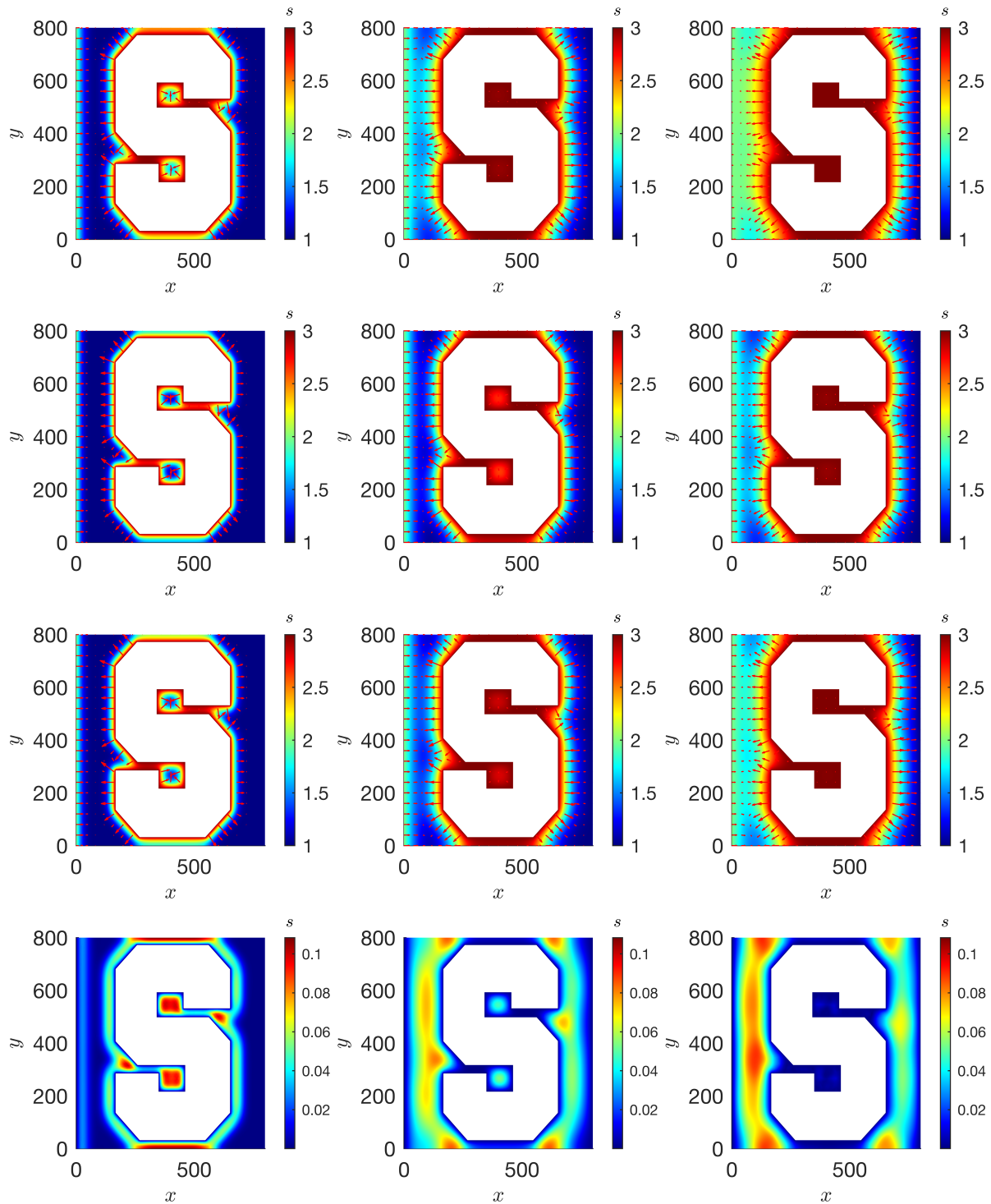


Figure 4: The training data at  $p^{(1)} = 1$  (first row),  $p^{(2)} = 2$  (second row), the reference solution at target parameter point  $p^* = 1.5$  (third row) and its corresponding DMD-PROM absolute error map (last row) are shown at times  $t = 500$  (left),  $t = 2500$  (middle) and  $t = 5000$  (right) for problem (4.9).

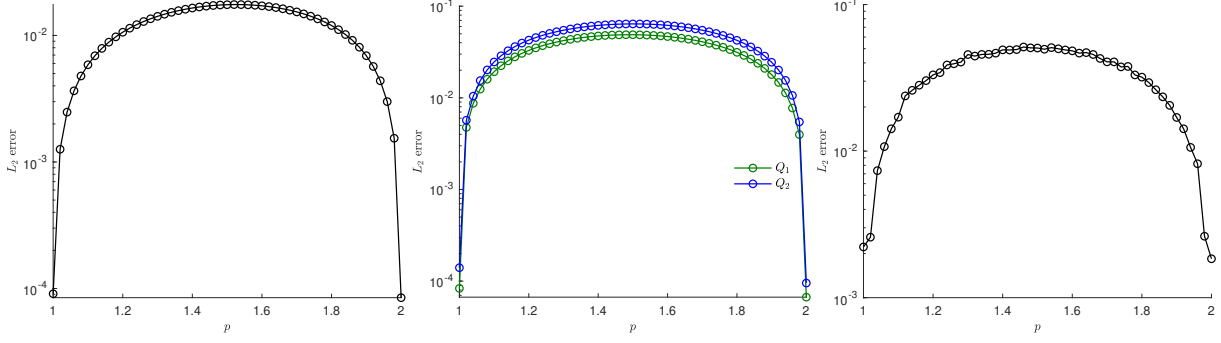


Figure 5: Left: Total  $L_2$  error (4.8) of  $r = 10$  rank DMD-PROM for QoIs  $\mathbf{Q} = \mathbf{S}$  with respect to different values of  $p^* \in [1, 2]$ ; Middle: Total  $L_2$  error (4.8) of  $r = 20$  rank DMD-PROM for QoIs  $\mathbf{Q}_1 = -k\partial_x\mathbf{S}$  and  $\mathbf{Q}_2 = -k\partial_y\mathbf{S}$  with respect to different values of  $p^* \in [1, 2]$ ; Right: Total  $L_2$  error (4.8) of  $r = 8$  rank DMD-PROM for the heat rate across the edge of interest  $\partial S_0$  with respect to different values of  $p^* \in [1, 2]$ .

### 4.3. Nonlinear Navier-Stokes Equation

We consider two-dimensional flow of an incompressible fluid with density  $\rho = 1$  and dynamic viscosity  $\nu = p \in [1/400, 1/800]$  (these and other quantities are reported in consistent units) around an impermeable circle of diameter  $D = 0.1$ . The flow, which takes place inside a rectangular domain  $\mathcal{D} = \{\mathbf{x} = (x, y)^\top : (x, y) \in [0, 2] \times [0, 1]\}$ , is driven by an externally imposed pressure gradient; the center of the circular inclusion is  $\mathbf{x}_{\text{circ}} = (0.3, 0.5)^\top$ . Dynamics of the three state variables, flow velocity  $\mathbf{s}(\mathbf{x}, t) = (s_1, s_2)^\top$  and fluid pressure  $P(\mathbf{x}, t)$ , is described by the two-dimensional Navier-Stokes equations,

$$\begin{cases} \frac{\partial s_1}{\partial x} + \frac{\partial s_2}{\partial y} = 0; \\ \frac{\partial s_1}{\partial t} + s_1 \frac{\partial s_1}{\partial x} + s_2 \frac{\partial s_1}{\partial y} = -\frac{1}{\rho} \frac{\partial P}{\partial x} + \nu \left( \frac{\partial^2 s_1}{\partial x^2} + \frac{\partial^2 s_1}{\partial y^2} \right), & \mathbf{x} \in \mathcal{D}, \quad t > 0; \\ \frac{\partial s_2}{\partial t} + u \frac{\partial s_2}{\partial x} + s_2 \frac{\partial s_2}{\partial y} = -\frac{1}{\rho} \frac{\partial P}{\partial y} + \nu \left( \frac{\partial^2 s_2}{\partial x^2} + \frac{\partial^2 s_2}{\partial y^2} \right); \end{cases} \quad (4.12)$$

subject to initial conditions  $\mathbf{s}(x, y, 0) = (0, 0)^\top$  and  $P(x, y, 0) = 0$ ; and boundary conditions

$$P(2, y, t) = 0, \quad \frac{\partial P}{\partial \mathbf{n}}|_{\partial \mathcal{D} \setminus \{x=2\}} = 0, \quad \mathbf{s}(0, y, t) = (1, 0)^\top, \quad \frac{\partial \mathbf{s}(2, y, t)}{\partial \mathbf{n}} = 0, \quad \mathbf{s}(x, 0, t) = \mathbf{s}(x, 1, t) = \mathbf{0}.$$

Here  $\mathbf{n}$  denotes the unit normal vector.

The training data and reference solution are obtained with the Matlab code [59], which implements a finite-difference scheme on the staggered grid with  $\Delta x = \Delta y = 0.02$  and  $\Delta t = 0.0015$ . Our QoIs are the magnitude of the flow velocity,  $\mathbf{Q}(t^n; p) = \sqrt{\mathbf{S}_1(t^n; p)^2 + \mathbf{S}_2(t^n; p)^2}$ , which follows a nonlinear equation in an implicit form. We collect  $N_{\text{snap}} = 250$  snapshots of  $\mathbf{Q}$  from  $t = 4.125$  to  $t = 4.5$  operated at  $p^{(1)} = 1/400$  and  $p^{(2)} = 1/800$  into the training dataset (shown in Figure), from which DMD learns the nonlinear dynamics from a 10-rank surrogate using the same observable as (4.5). This construction is equivalent to the xDMD and the same numerical example was shown in section 4.3 of [24]. The reference

solution of a particular test parameter point  $p^* = 1.5$ , together with the absolute error map of the DMD-PROM, are presented in Figure 7.

Figure 8 shows the accuracy of the 10-rank DMD-PROM for different values of  $p^* \in [1/400, 1/800]$ . Another alternative approach to tackle this problem is Kriging. Kriging interpolates the velocity magnitude map pixel by pixel based on prior covariances, which depend on the distance between the target point and the sampled points in the parameter space. It is a pure data-driven approach in the sense that it does not take the underlying governing equations into account. Although Kriging is widely used in many applications (most linear problems) successfully, previous study [34] demonstrates that such pure data-driven approach may fail to detect the bifurcations in a complex dynamic system. Figure 7 and 8 also verify the disadvantage of Kriging in accurately capturing the complex nonlinear dynamics compared to the physics-aware DMD-PROM.

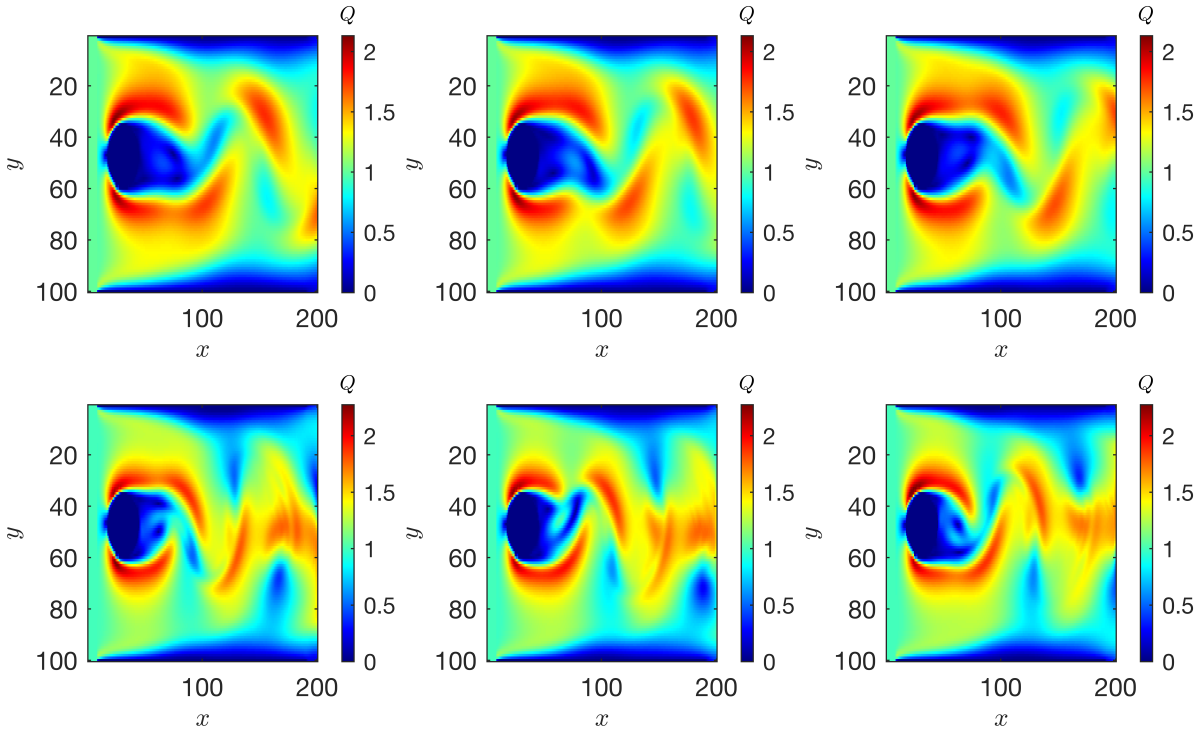


Figure 6: The training data of (4.12) at  $p^{(1)} = 1/400$  (top row) and  $p^{(2)} = 1/800$  (bottom row), at times  $t = 4.125$  (left),  $t = 4.3125$  (middle) and  $t = 4.5$  (right).

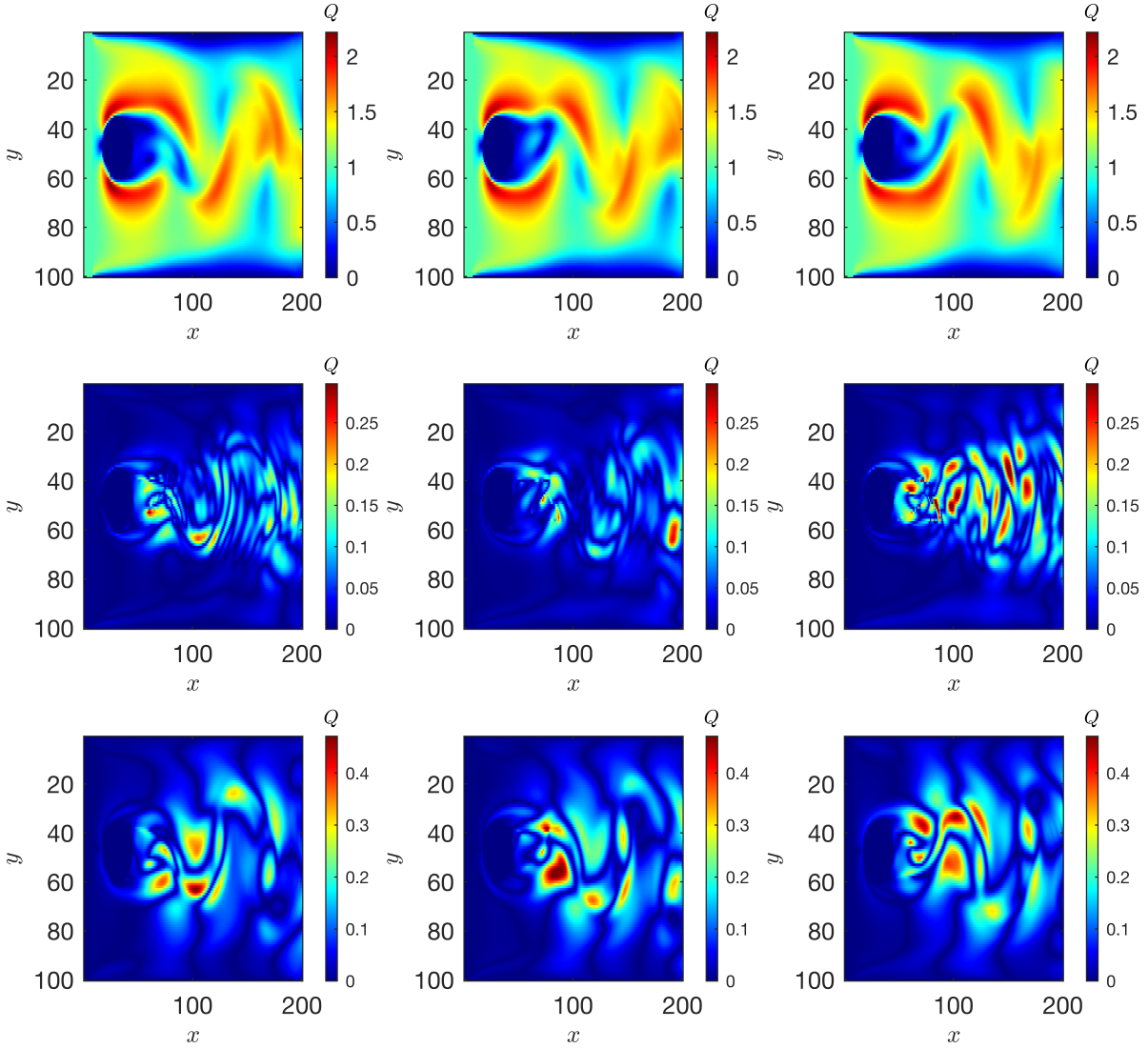


Figure 7: The reference solution (top row) of (4.12), corresponding DMD-PROM absolute error map (middle row) and Kriging absolute error map (bottom row) at target parameter point  $p^* = 1/600$ , at times  $t = 4.125$  (left),  $t = 4.3125$  (middle) and  $t = 4.5$  (right).

Table 1 shows the comparison of computational costs in exploring the dynamics with different parameter values  $p^* \in [1/800, 1/400]$  using the HFM, Kriging and DMD-PROM respectively. The parameter space of interests is discretized into 51 uniformly distributed points, including the 2 endpoints (used as training parameter samples) and the rest 49 inner points (used as test parameter points). Although Kriging has a larger online speedup, the proposed DMD-PROM has the same level total speedup as Kriging and much better accuracy in all test parameter points as shown in Figure 8.

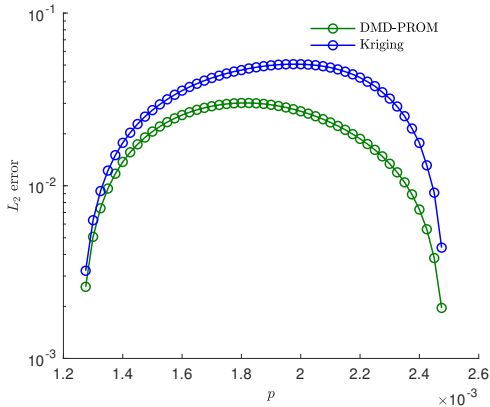


Figure 8: Total  $L_2$  error (4.8) of  $r = 10$  rank DMD-PROM (blue) and Kriging (green) for QoIs  $\mathbf{Q} = \sqrt{\mathbf{S}_1(t^n; p)^2 + \mathbf{S}_2(t^n; p)^2}$  with respect to different values of  $p^* \in [1/800, 1/400]$ .

Table 1: Comparison of computational performances

Approach	HFM	Kriging	DMD-PROM
Offline(seconds)	–	15.2195	14.0906
Online (seconds)	255.1326	1.5288	2.8567
Online speedup	–	167	89
Total speedup	–	15	15

## 5. Conclusion

In this work, we propose a new physics-aware data-driven framework of model reduction for parametric complex systems. It combines the advantages of the popular data-driven modeling tool DMD and previous studies on manifold interpolations over the parameter space of interests. The novelty of this work includes: 1. alleviating the strict constraints on the access to the HFMs of the high dimensional state variables in projection-based PROM methods by constructing low-dimensional surrogate models for the QoIs directly in a physics-aware data-driven way; 2. improving the PROM accuracy from conventional pure-data driven tools like Kriging and requiring much less training data from modern nonlinear ML tools like deep learning. The proposed framework shows robustness and flexibility by providing a bridge between the understanding of data and physics. The significant speedup also verifies that DMD-PROM is suitable for real-time processing.

In the follow-up studies we will develop the current framework in the following directions: 1). To further improve the online speedup, more efficient manifold interpolation methods (e.g., [37]) need to be explored; 2). For problems in high-dimensional parameter spaces, adaptive sampling strategies need to be carefully designed and the current framework needs to be applied together with practical considerations of parameter space reduction [60]; 3). Further studies on error estimation of the whole framework are needed in order to construct reliable surrogate models, which may further enable outer-loop applications such as design, inverse problems, optimization and uncertainty quantification.

## SUPPLEMENTAL MATERIAL

---

**Algorithm S1:** POD-PROM framework for linear system (4.4)

---

*Offline Step:*

**For**  $i = 1, \dots, N_{\text{MC}}$ ,

    Compute the high fidelity training data (2.6),

    Input:  $\{\mathbf{Q}(t_0; \mathbf{p}^{(i)}), \dots, \mathbf{Q}(t_{N_{\text{snap}}}; \mathbf{p}^{(i)})\}$ ,  $\mathbf{A}(p^{(i)})$  and  $\mathbf{b}(p^{(i)})$ ,

1. Apply SVD  $[\mathbf{Q}(t_0; \mathbf{p}^{(i)})^\top, \dots, \mathbf{Q}(t_{N_{\text{snap}}}; \mathbf{p}^{(i)})^\top]^\top \approx \mathbf{V}(\mathbf{p}^{(i)})\boldsymbol{\Sigma}(\mathbf{p}^{(i)})\mathbf{Z}(\mathbf{p}^{(i)})^*$  with  $\mathbf{V}(\mathbf{p}^{(i)}) \in \mathbb{C}^{N \times r}$ ,  $\boldsymbol{\Sigma}(\mathbf{p}^{(i)}) \in \mathbb{C}^{r \times r}$ ,  $\mathbf{Z}(\mathbf{p}^{(i)}) \in \mathbb{C}^{r \times N_{\text{snap}}}$ , where  $r$  is the truncated rank chosen by certain criteria and should be the same for all  $i = 1, \dots, N_{\text{MC}}$ .

2. Use Galerkin-projection to compute local ROMs:

$$\mathbf{A}_r(p^{(i)}) = \mathbf{V}(p^{(i)})^\top \mathbf{A}(p^{(i)}) \mathbf{V}(p^{(i)}), \mathbf{b}_r(p^{(i)}) = \mathbf{V}(p^{(i)})^\top \mathbf{b}(p^{(i)}), \quad (\text{S1})$$

3. Compute  $\mathbf{P}^{(i,j)} = \mathbf{V}(\mathbf{p}^{(i)})^\top \mathbf{V}(\mathbf{p}^{(j)})$  for  $i, j = 1, \dots, N_{\text{MC}}$ .

    Output:  $\mathbf{V}(\mathbf{p}^{(i)})$ ,  $\mathbf{P}^{(i,j)}$ ,  $\mathbf{A}_r(\mathbf{p}^{(i)})$  and  $\mathbf{b}_r(\mathbf{p}^{(i)})$ .

**End**

*Online Step:*

- Interpolation of ROBs:

$$\text{Input: } \{\mathbf{V}(\mathbf{p}^{(i)})\}_{i=1}^{N_{\text{MC}}}, \{\mathbf{P}^{(i,j)}\}_{i,j=1}^{N_{\text{MC}}}, \{\mathbf{p}^{(i)}\}_{i=1}^{N_{\text{MC}}}, \mathbf{p}^* \xrightarrow{\text{Algorithm 2}} \text{Output: } \mathbf{V}(\mathbf{p}^*)$$

- Interpolation of PROMs:

$$\text{Input: } \{\mathbf{A}_r(\mathbf{p}^{(i)})\}_{i=1}^{N_{\text{MC}}}, \{\mathbf{P}^{(i,j)}\}_{i,j=1}^{N_{\text{MC}}}, \text{ reference choice } i_0 \xrightarrow{\text{Algorithm 3\& 4}} \text{Output: } \mathbf{A}_r(\mathbf{p}^*)$$

$$\text{Input: } \{\mathbf{b}_r(\mathbf{p}^{(i)})\}_{i=1}^{N_{\text{MC}}}, \{\mathbf{P}^{(i,j)}\}_{i,j=1}^{N_{\text{MC}}}, \text{ reference choice } i_0 \xrightarrow{\text{Algorithm 3\& 4}} \text{Output: } \mathbf{b}_r(\mathbf{p}^*)$$

- POD reconstruction:

    Input:  $\mathbf{A}_r(\mathbf{p}^*)$ ,  $\mathbf{b}_r(\mathbf{p}^*)$ ,  $\mathbf{V}(\mathbf{p}^*)$  and  $\mathbf{Q}(t_0; \mathbf{p}^*)$ ,

$$\mathbf{q}(t_0; \mathbf{p}^*) = \mathbf{V}(\mathbf{p}^*)^\top \mathbf{Q}(t_0; \mathbf{p}^*)$$

**For**  $k = 1, \dots, N_T$ ,

$$\mathbf{q}(t_k; \mathbf{p}^*) = \mathbf{A}_r(p^*)\mathbf{q}(t_{k-1}; \mathbf{p}^*) + \mathbf{b}_r(p^*), \quad \mathbf{Q}_{\text{POD}}(t_k; \mathbf{p}^*) = \mathbf{V}(\mathbf{p}^*)\mathbf{q}(t_k; \mathbf{p}^*)$$

**End**

    Output:  $\mathbf{Q}_{\text{POD}}(t_k; \mathbf{p}^*)$ .

---

## Reference

- [1] P. Benner, S. Gugercin, K. Willcox, A survey of projection-based model reduction methods for parametric dynamical systems, *SIAM review* 57 (4) (2015) 483–531.
- [2] J. L. Lumley, The structure of inhomogeneous turbulent flows, *Atmospheric turbulence and radio wave propagation* (1967).
- [3] G. Kerschen, J.-c. Golinval, A. F. Vakakis, L. A. Bergman, The method of proper orthogonal decomposition for dynamical characterization and order reduction of mechanical systems: an overview, *Nonlinear dynamics* 41 (1) (2005) 147–169.
- [4] S. Chaturantabut, D. C. Sorensen, Nonlinear model reduction via discrete empirical interpolation, *SIAM Journal on Scientific Computing* 32 (5) (2010) 2737–2764.
- [5] C. W. Rowley, Model reduction for fluids, using balanced proper orthogonal decomposition, *International Journal of Bifurcation and Chaos* 15 (03) (2005) 997–1013.
- [6] B. Moore, Principal component analysis in linear systems: Controllability, observability, and model reduction, *IEEE transactions on automatic control* 26 (1) (1981) 17–32.
- [7] S. Gugercin, A. C. Antoulas, C. Beattie, H<sub>2</sub> model reduction for large-scale linear dynamical systems, *SIAM journal on matrix analysis and applications* 30 (2) (2008) 609–638.
- [8] A. C. Antoulas, C. A. Beattie, S. Güğercin, *Interpolatory methods for model reduction*, SIAM, 2020.
- [9] K. Lee, K. T. Carlberg, Model reduction of dynamical systems on nonlinear manifolds using deep convolutional autoencoders, *Journal of Computational Physics* 404 (2020) 108973.
- [10] C. E. Rasmussen, Gaussian processes in machine learning, in: *Summer school on machine learning*, Springer, 2003, pp. 63–71.
- [11] G. S. H. Pau, Y. Zhang, S. Finsterle, Reduced order models for many-query subsurface flow applications, *Computational Geosciences* 17 (4) (2013) 705–721.
- [12] D. Booker, R. Woods, Comparing and combining physically-based and empirically-based approaches for estimating the hydrology of ungauged catchments, *Journal of Hydrology* 508 (2014) 227–239.
- [13] S. A. Naghibi, H. R. Pourghasemi, B. Dixon, Gis-based groundwater potential mapping using boosted regression tree, classification and regression tree, and random forest machine learning models in iran, *Environmental monitoring and assessment* 188 (1) (2016) 1–27.

- [14] P. J. Schmid, Dynamic mode decomposition of numerical and experimental data, *Journal of fluid mechanics* 656 (2010) 5–28.
- [15] J. N. Kutz, S. L. Brunton, B. W. Brunton, J. L. Proctor, *Dynamic mode decomposition: data-driven modeling of complex systems*, SIAM, 2016.
- [16] B. Peherstorfer, K. Willcox, Data-driven operator inference for nonintrusive projection-based model reduction, *Computer Methods in Applied Mechanics and Engineering* 306 (2016) 196–215.
- [17] S. A. McQuarrie, P. Khodabakhshi, K. E. Willcox, Non-intrusive reduced-order models for parametric partial differential equations via data-driven operator inference, *arXiv preprint arXiv:2110.07653* (2021).
- [18] J. S. Hesthaven, S. Ubbiali, Non-intrusive reduced order modeling of nonlinear problems using neural networks, *Journal of Computational Physics* 363 (2018) 55–78.
- [19] T. Qin, K. Wu, D. Xiu, Data driven governing equations approximation using deep neural networks, *Journal of Computational Physics* 395 (2019) 620–635.
- [20] J. Nathan Kutz, J. L. Proctor, S. L. Brunton, Applied koopman theory for partial differential equations and data-driven modeling of spatio-temporal systems, *Complexity* 2018 (2018).
- [21] H. Lu, D. M. Tartakovsky, Lagrangian dynamic mode decomposition for construction of reduced-order models of advection-dominated phenomena, *J. Comput. Phys.* (2020) 109229.
- [22] H. Lu, D. M. Tartakovsky, Prediction accuracy of dynamic mode decomposition, *SIAM Journal on Scientific Computing* 42 (3) (2020) A1639–A1662.
- [23] H. Lu, D. M. Tartakovsky, Dynamic mode decomposition for construction of reduced-order models of hyperbolic problems with shocks, *Journal of Machine Learning for Modeling and Computing* 2 (1) (2021).
- [24] H. Lu, D. M. Tartakovsky, Extended dynamic mode decomposition for inhomogeneous problems, *Journal of Computational Physics* 444 (2021) 110550.
- [25] M. Raissi, P. Perdikaris, G. E. Karniadakis, Physics-informed neural networks: A deep learning framework for solving forward and inverse problems involving nonlinear partial differential equations, *Journal of Computational physics* 378 (2019) 686–707.
- [26] G. E. Karniadakis, I. G. Kevrekidis, L. Lu, P. Perdikaris, S. Wang, L. Yang, Physics-informed machine learning, *Nature Reviews Physics* 3 (6) (2021) 422–440.



- [27] Y. Zhu, N. Zabaras, P.-S. Koutsourelakis, P. Perdikaris, Physics-constrained deep learning for high-dimensional surrogate modeling and uncertainty quantification without labeled data, *Journal of Computational Physics* 394 (2019) 56–81.
- [28] E. Qian, B. Kramer, B. Peherstorfer, K. Willcox, Lift & learn: Physics-informed machine learning for large-scale nonlinear dynamical systems, *Physica D: Nonlinear Phenomena* 406 (2020) 132401.
- [29] B. Epureanu, A parametric analysis of reduced order models of viscous flows in turbomachinery, *Journal of fluids and structures* 17 (7) (2003) 971–982.
- [30] C. Homescu, L. R. Petzold, R. Serban, Error estimation for reduced-order models of dynamical systems, *SIAM Journal on Numerical Analysis* 43 (4) (2005) 1693–1714.
- [31] R. Serban, C. Homescu, L. R. Petzold, The effect of problem perturbations on nonlinear dynamical systems and their reduced-order models, *SIAM Journal on Scientific Computing* 29 (6) (2007) 2621–2643.
- [32] T. Lieu, C. Farhat, Adaptation of aeroelastic reduced-order models and application to an f-16 configuration, *AIAA journal* 45 (6) (2007) 1244–1257.
- [33] D. Amsallem, C. Farhat, Interpolation method for adapting reduced-order models and application to aeroelasticity, *AIAA journal* 46 (7) (2008) 1803–1813.
- [34] D. Amsallem, C. Farhat, An online method for interpolating linear parametric reduced-order models, *SIAM Journal on Scientific Computing* 33 (5) (2011) 2169–2198.
- [35] N. T. Son, A real time procedure for affinely dependent parametric model order reduction using interpolation on grassmann manifolds, *International Journal for Numerical Methods in Engineering* 93 (8) (2013) 818–833.
- [36] R. Zimmermann, A locally parametrized reduced-order model for the linear frequency domain approach to time-accurate computational fluid dynamics, *SIAM Journal on Scientific Computing* 36 (3) (2014) B508–B537.
- [37] R. Zhang, S. Mak, D. Dunson, Gaussian process subspace regression for model reduction, *arXiv preprint arXiv:2107.04668* (2021).
- [38] H. Lu, D. Ermakova, H. M. Wainwright, L. Zheng, D. M. Tartakovsky, Data-informed emulators for multi-physics simulations, *Journal of Machine Learning for Modeling and Computing* 2 (2) (2021).
- [39] K. Bhattacharya, B. Hosseini, N. B. Kovachki, A. M. Stuart, Model reduction and neural networks for parametric pdes, *The SMAI journal of computational mathematics* 7 (2021) 121–157.

- [40] P. Sentz, K. Beckwith, E. C. Cyr, L. N. Olson, R. Patel, Reduced basis approximations of parameterized dynamical partial differential equations via neural networks, arXiv preprint arXiv:2110.10775 (2021).
- [41] S. L. Brunton, B. W. Brunton, J. L. Proctor, J. N. Kutz, Koopman invariant subspaces and finite linear representations of nonlinear dynamical systems for control, PloS one 11 (2) (2016) e0150171.
- [42] J. H. Tu, Dynamic mode decomposition: Theory and applications, Ph.D. thesis, Princeton University (2013).
- [43] M. Schmidt, H. Lipson, Distilling free-form natural laws from experimental data, science 324 (5923) (2009) 81–85.
- [44] W.-X. Wang, R. Yang, Y.-C. Lai, V. Kovanis, C. Grebogi, Predicting catastrophes in nonlinear dynamical systems by compressive sensing, Physical review letters 106 (15) (2011) 154101.
- [45] M. O. Williams, C. W. Rowley, I. G. Kevrekidis, A kernel-based approach to data-driven koopman spectral analysis, arXiv preprint arXiv:1411.2260 (2014).
- [46] Q. Li, F. Dietrich, E. M. Bollt, I. G. Kevrekidis, Extended dynamic mode decomposition with dictionary learning: A data-driven adaptive spectral decomposition of the koopman operator, Chaos: An Interdisciplinary Journal of Nonlinear Science 27 (10) (2017) 103111.
- [47] P.-A. Absil, R. Mahony, R. Sepulchre, Riemannian geometry of grassmann manifolds with a view on algorithmic computation, Acta Applicandae Mathematica 80 (2) (2004) 199–220.
- [48] W. M. Boothby, W. M. Boothby, An introduction to differentiable manifolds and Riemannian geometry, Revised, Vol. 120, Gulf Professional Publishing, 2003.
- [49] S. Helgason, Differential geometry, lie groups, and symmetric spaces. ams, Graduate Texts in Mathematics (2001).
- [50] I. U. Rahman, I. Drori, V. C. Stodden, D. L. Donoho, P. Schröder, Multiscale representations for manifold-valued data, Multiscale Modeling & Simulation 4 (4) (2005) 1201–1232.
- [51] A. Edelman, T. A. Arias, S. T. Smith, The geometry of algorithms with orthogonality constraints, SIAM journal on Matrix Analysis and Applications 20 (2) (1998) 303–353.
- [52] R. M. Wald, General relativity(book), Chicago, University of Chicago Press, 1984, 504 p (1984).
- [53] M. P. Do Carmo, J. Flaherty Francis, Riemannian geometry, Vol. 6, Springer, 1992.
- [54] H. Späth, One dimensional spline interpolation algorithms, AK Peters/CRC Press, 1995.

- [55] C. De Boor, A. Ron, Computational aspects of polynomial interpolation in several variables, *Mathematics of Computation* 58 (198) (1992) 705–727.
- [56] C. F. Van Loan, G. Golub, *Matrix computations* (johns hopkins studies in mathematical sciences), Matrix Computations (1996).
- [57] D. J. Ewins, *Modal testing: theory, practice and application*, John Wiley & Sons, 2009.
- [58] M. O. Williams, I. G. Kevrekidis, C. W. Rowley, A data-driven approximation of the koopman operator: Extending dynamic mode decomposition, *Journal of Nonlinear Science* 25 (6) (2015) 1307–1346.
- [59] J. Johns, A Matlab code for numerical solution of Navier-Stokes equations for two-dimensional incompressible flow (velocity-pressure formulation) along with ability for importing custom scenarios for the fluid flow, <https://github.com/JamieMJohns/Navier-stokes-2D-numerical-solve-incompressible-flow-with-custom-scenarios-MATLAB> (2018).
- [60] C. Lieberman, K. Willcox, O. Ghattas, Parameter and state model reduction for large-scale statistical inverse problems, *SIAM Journal on Scientific Computing* 32 (5) (2010) 2523–2542.